Characterizing a Resonator Bolometer Array

Thesis by

Rebecca Wernis

In Partial Fulfillment of the Requirements

for the Degree of

Bachelor of Science

California Institute of Technology

Pasadena, California

2013

(Defended May 14, 2013)

Acknowledgements

No one does research in a vacuum – especially not experimental physicists. Since joining the Zmiudzinas research group in June 2011 I've had help in every step of the work presented here. I would first like to thank Prof. Jonas Zmuidzinas for offering me a place in his research group for two years, where I could learn firsthand and take part in all the work that goes into detector development. Next I would like to thank Loren Swenson, a postdoc in Jonas' group who brought me from a state of knowing nothing about microwave electronics and cryogenics to the point where I could set up and program the instruments and take data on my own. Loren was always available when I had questions or needed help and worked closely with me not only in the data taking but the analysis and interpretation as well, drawing on his considerable knowledge and experience in the field.

From time to time I have had assistance from several other researchers, namely Chris McKenney, Peter Day, Darren Dowell and Matt Hollister. Thanks also to Peter Day, Byeong Ho Eom, and Rick LeDuc at JPL for the fabrication and initial testing of the resonator bolometer array.

Abstract

High-background applications such as climate monitoring, biology and security applications demand a large dynamic range. Under such conditions ultra-high sensitivity is not required. The resonator bolometer is a novel detector which is well-suited for these conditions. This device takes advantage of the high-density frequency multiplexing capabilities of superconducting microresonators while allowing for the use of high-Tc superconductors in fabrication, which enables a modest (1-4 K) operating temperature and larger dynamic range than is possible with conventional microresonators. The moderate operating temperature and intrinsic multiplexability of this device reduce cost and allow for large pixel counts, making the resonator bolometer especially suitable for the aforementioned applications. A single pixel consists of a superconducting microresonator whose light-absorbing area is placed on a thermally isolated island. Here we present experimental results and theoretical calculations for a prototype resonator bolometer array. Intrinsic device noise and noise equivalent power (NEP) under both dark and illuminated conditions are presented. Under dark conditions the device sensitivity is limited by the thermal noise fluctuations from the bolometer legs. Under the experimental illuminated conditions the device was photon noise limited.

Contents

List of Figures

Chapter 1

Background

Cryogenic detectors for photon detection have applications in astronomy, cosmology, particle physics, climate science, chemistry, security and more. In the infrared and submillimeter wavelengths, the most widely used sensor type is the bolometer, which employs a very sensitive thermometer to measure small temperature changes on a thermally isolated absorber. Over the past decade, however, interest has grown in superconducting microresonators for use as photon detectors because of their simplicity and potential to be multiplexed in large arrays. I have investigated and characterized a novel prototype device which incorporates elements of both bolometers and superconducting microresonators in its design. This resonator bolometer takes advantage of the scalability offered by the use of superconducting microresonator technology along with the versatility offered by the use of a thermally insulated island. Because of its unique potential, the resonator bolometer is proving promising for many different science applications. In order to discuss these further it will be necessary to first outline the basic operating principles of bolometer-based detectors and superconducting microresonators.

1.1 Introduction to bolometers

The bolometer concept is ubiquitous in infrared sensor design. The basic setup consists of an absorbing element with heat capacity C which is attached to a heat sink by thin legs which have a combined thermal conductance G (Fig. 1.1). The heat sink is well thermally sunk so as to maintain a constant base temperature from which the isolated absorbing element's temperature will deviate. When a power source P is turned on, the absorbing element's temperature rises to a limiting value of $T_{\mathrm{sink}} + P/G$ with time constant $\tau_{\mathrm{th}} = C/G$. A thermometer placed on the island measures this change. When the power source is turned off, the island temperature decays to the bath temperature with the same time constant.

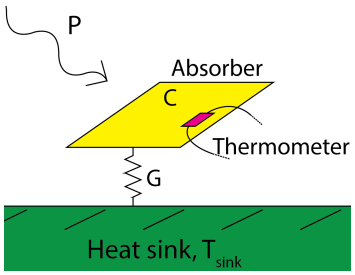

Figure 1.1: Schematic diagram of a bolometer pixel. A thermometer measures the temperature change associated with a change in incident power P on the absorber with heat capacity C. Heat escapes to the substrate via thin legs with combined thermal conductance G.

1.1.1 Bolometer modeling

The quantities C, G and the noise equivalent power in a bolometer may be calculated in terms of fundamental dimensions and properties of the device. The heat capacity of a slab of material of mass m, density ρ and specific heat c is given by

$$C = \frac{mc}{\rho}.$$

The thermal conductance of a wire with length l, cross-sectional area A and resistivity ρ is given by

$$G = \frac{\rho A}{l}.$$

Quantized fluctuations in the thermal energy flowing across the legs introduce phonon noise. The phonon noise contribution to the noise equivalent power is given by

$$\mathrm{NEP}_{\mathrm{phonon}} = \sqrt{4kT^2G}$$

in units of $\mathrm{W}/\sqrt{\mathrm{Hz}}$ [13].

1.2 Introduction to superconducting microresonators

Superconducting microresonators are of interest for use in sensitive photon detection [5], direct detection of dark matter [12] and quantum information experiments [14] among other applications [15]. Their simple fabrication process, involving a single deposition of a patterned superconducting film on an insulator substrate, and natural frequency domain multiplexing make them attractive candidates for large scale ($\sim 10^6$ pixel) arrays.

1.2.1 Microresonator electrodynamics

True to their name superconducting microresonators have zero resistance for direct currents when cooled below their superconducting transition temperature T_c. This supercurrent is carried by pairs of electrons, called Cooper pairs, with binding energy $2\Delta \approx 3.5 k_B T_c$ for $T \ll T_c$ [2]. However, for alternating currents energy may be stored as kinetic energy in the Cooper pairs and may be recovered without loss by reversing the electric field. Thin (10s to 100s of nanometers) superconducting films additionally permit energy to be transferred between Cooper pair motion and the magnetic field, since magnetic fields penetrate below the surface of superconductors a distance λ, called the London penetration depth, which is typically of order the thickness of the film. This reactive energy flow results in a surface kinetic inductance $L_s = \mu_0 \lambda$.

Additionally a dissipative component to the conductivity is present due to the small fraction of electrons not bound up in Cooper pairs, called quasiparticles, which behave as normal electrons (i.e. they do not carry the supercurrent). The presence of quasiparticles and the finite inertia of the Cooper pairs result in a complex conductivity $\sigma(\omega) = \sigma_1(\omega) - i\sigma_2(\omega)$ as described by the Mattis-Bardeen theory [10]. Any energy input $E > 2\Delta$ which breaks a Cooper pair into quasiparticles will introduce a corresponding perturbation in the complex conductivity $\delta\sigma$. This perturbation may be measured very precisely by constructing a resonant circuit.

1.2.2 Principles of operation

Superconducting microresonator detectors are typically either a quarter-wave transmission line resonator or a lumped-element circuit. A single coplanar waveguide (CPW) transmission line is coupled to every pixel in the array. The superconducting material is carefully chosen so that the resonators exhibit very low loss in each oscillation; quality factors of $Q \sim 10^5$ are readily obtainable. Since the device studied in this paper utilizes the lumped-element pixels, I will focus my discussion on that design. A lumped-element pixel consists of a capacitor and inductor in series which are capacitively coupled to the transmission line (Fig. 1.2a). By varying the capacitor area, the capacitance and thus the characteristic resonant frequency of the pixel may be varied in a controlled manner according to $\omega = (LC)^{-1/2}$.

When sufficient energy is absorbed by the resonator, the resistance and reactance change according to the change in conductivity $\delta\sigma$ as described above. By varying the frequency of the current on the feedline and thus sampling many points near and within the resonance, the dissipation and phase changes may be quantified and the original absorbed energy determined. Because the phase and dissipation directions are orthogonal, one can use one or the other or both to determine the optical signal change.

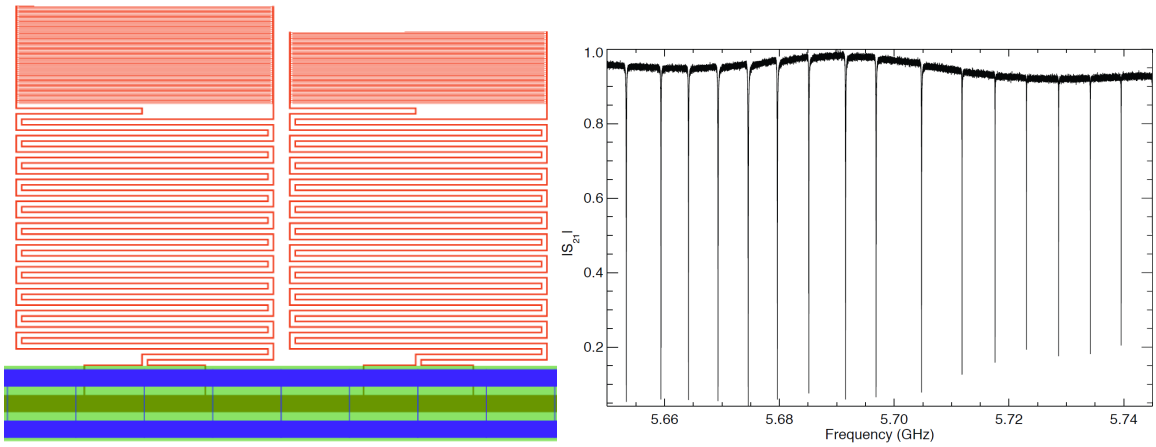

(a) Lumped-element pixels (Image courtesy of C. McKenney)

(b) Sample normalized signal amplitude readout

Figure 1.2: (a) An example of the lumped-element design. The interdigitated capacitor, top, can be varied in size to control the resonant frequency of the pixel. In the center, the meandered inductor, which acts as the photon absorber, takes up most of the pixel area. The coplanar waveguide, along which the microwave signal travels, is visible at the bottom. (b) Signal transmission vs. frequency using standard scattering matrix notation. Each dip in transmission indicates attenuation from a resonant pixel coupled to the transmission line.

1.2.3 Frequency multiplexing

By tuning each pixel to a different resonant frequency, multiple pixels may be read out simply by varying the AC frequency on the feedline (Fig. 1.2b). Only this single feedline is required to read out the entire array. Pixels may be engineered to be closely spaced in frequency, in principle allowing hundreds to thousands of pixels coupled to a single feedline. Furthermore, the readout technology required for such large arrays already exists. One example is the CASPER ROACH processing board shown in Fig. 1.3 [4]. One system is currently being used to read out the 32 x 32 pixel ARray Camera for Optical to Near-infrared Spectrophotometry (ARCONS) [11].

1.2.4 Photon absorption

Most often either direct radiation coupling or an antenna structure which focuses radiation to the sensitive part of the resonator is used to absorb photons. In the direct detection case, the inductor serves as the photon-sensitive area, and absorbed photons directly break Cooper pairs and thus modify the inductance and resistance. For wavelengths $\lambda \gg s$, the spacing between lines of the inductor, the absorbing area acts as a sheet resistance, whose value depends on the fraction of the pixel area covered by superconducting film. The array is back-illuminated, with light first passing through the silicon substrate before contacting a pixel, for better impedance matching between the pixels and free space.

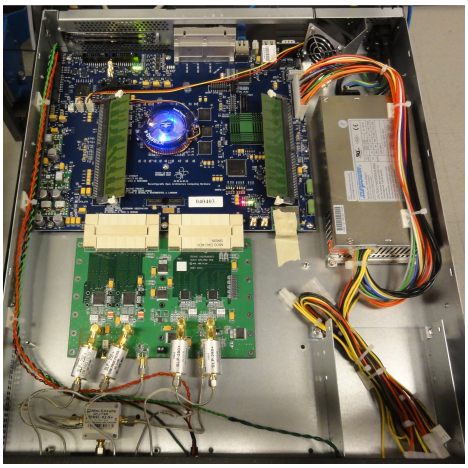

Figure 1.3: A Reconfigurable Open Architecture Computing Hardware (ROACH) board used to read out large superconducting microresonator arrays.

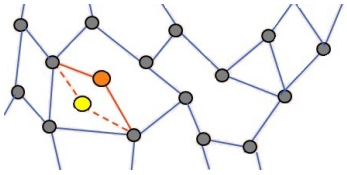

Figure 1.4: Two level systems, in which an atom may quantum tunnel between two local minima in potential energy, are hosted in a thin amorphous surface layer on the crystalline substrate. They introduce excess noise in the position of the resonant frequency in a resonant circuit.

1.2.5 Two level systems

In practice, superconducting microresonators exhibit excess noise in the frequency (phase) direction not predicted by superconductivity theory. This noise arises from the presence of an amorphous surface layer on the crystalline substrate on which the superconducting material is deposited. This layer appears when the atoms on the surface of the crystal contact air and form bonds with molecules in the air. Because of irregularities in the structure of this surface layer, under the presence of a strong electric field an atom or group of atoms may quantum tunnel from one local minimum in potential energy to another (Fig. 1.4). The moving atoms carry a dipole moment so that these two level systems (TLS) contribute randomly to the dielectric constant of the capacitor in the resonant circuit and thus the capacitance and the resonant frequency. While a microscopic theory of the noise introduced by TLS does not yet exist, the effect is well-documented in experiments [3, 5, 8] and a semi-empirical model has been developed by Gao et. al. [7]. This model may be used to design devices which minimize the TLS noise.

1.3 The resonator bolometer

Superconducting microresonators are revolutionary devices but they do not come without limitations. They must operate at temperatures $T \ll T_c$, where the surface inductance dominates. To operate in the 1 - 4K temperature range, desirable for its simple cooling requirements compared to sub-Kelvin temperatures, superconductors with $T_c \sim 15K$ must be used. However, superconductors with such high transition temperatures have short quasiparticle lifetimes [9]. The quasiparticle lifetime, or the time it takes for quasiparticles to recombine once formed, limits the sensitivity of a detector. For constant illumination, a shorter lifetime implies fewer quasiparticles at a given time and thus a smaller signal. Thus microresonators must operate at sub-Kelvin temperatures to remain sensitive.

Along with my collaborators at Caltech and NASA's Jet Propulsion Laboratory I have investigated placing the sensitive portion of the resonator on a thermally insulated island as a way to circumvent this obstacle. In the resonator bolometer, the inductor is placed on the bolometer island, where it acts as both the photon absorber and the thermometer measuring the energy trapped on the island. The rest of the circuit is deposited directly onto the substrate (Fig. 1.5a). This design effectively extends the quasiparticle lifetime because thermal energy released from the recombination of a pair of quasiparticles is trapped on the island, where it may break another Cooper pair (Fig. 1.5b). The magnitude of the signal is thus governed by heat flow from the bolometer island legs to the substrate instead of by the quasiparticle recombination time. In contrast, in a superconducting film deposited directly on the substrate, the emitted thermal energy, or phonon, simply escapes to the substrate, and only incident photons break Cooper pairs.

The resonator bolometer design thus allows for a broad class of superconducting materials to be used in fabrication. It additionally enables a straightforward decoupling of the meander from photon detection; a separate absorber could easily be placed on a bolometer island with a resonator inductor, with the resonator detecting the thermal energy produced by this absorber.

This design has many potential science applications. The ability to operate at temperatures above 1K makes the resonator bolometer attractive for space-based instrumentation because of the greatly simplified cryogenic setup. It is especially suitable for high-background applications such as Earth observation in the far-infrared because of the tunability of the dynamic range enabled by the use of high-T_c superconductors. The investigation into the viability of the bolometric island as a coupling mechanism is important for further development of superconducting microresonator-based designs for gamma ray, X-ray and particle detectors.

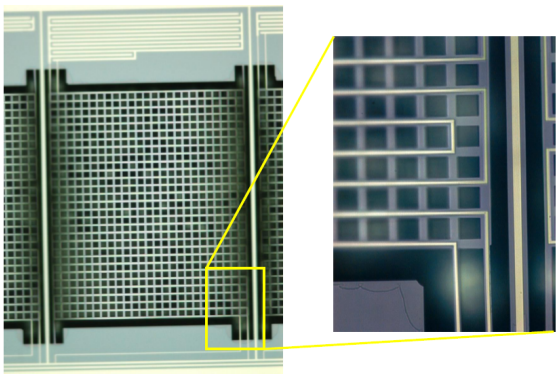

(a) Resonator bolometer pixel

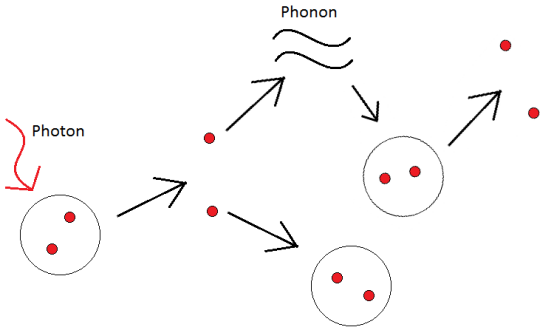

(b) Energy recycling in a resonator bolometer pixel

Figure 1.5: (a) A resonator bolometer pixel. The inductor is on a wire mesh grid released from the substrate and connected to it via six legs (see closeup). The capacitor (top) and the CPW (bottom) are both directly on the substrate. (b) Energy recycling in a resonator bolometer pixel. An incident photon breaks a Cooper pair into its constituent quasiparticles, which quickly recombine. The energy from recombination is emitted as a phonon. Since the phonon is trapped on the isolated island, it is available to break another Cooper pair. Overall, a given input power causes more quasiparticles to exist at a given time than if the sensitive portion of the pixel were not thermally isolated, so that the signal is larger.

1.3.1 Fabrication

In order to begin investigating the feasibility of the resonator bolometer concept, a prototype array was fabricated at NASA's Jet Propulsion Laboratory (Fig. 1.6). This array consists of a single row of 16 pixels in two frequency bands. The chosen superconducting material is NbTiN, with a T_c of approximately 14 K. The NbTiN was deposited and patterned on a layer of silicon nitride on the silicon substrate. Next, trenches in the silicon were etched to isolate neighboring pixels. Finally, the silicon was etched away from underneath the grid mesh to suspend the inductors and thus thermally isolate them.

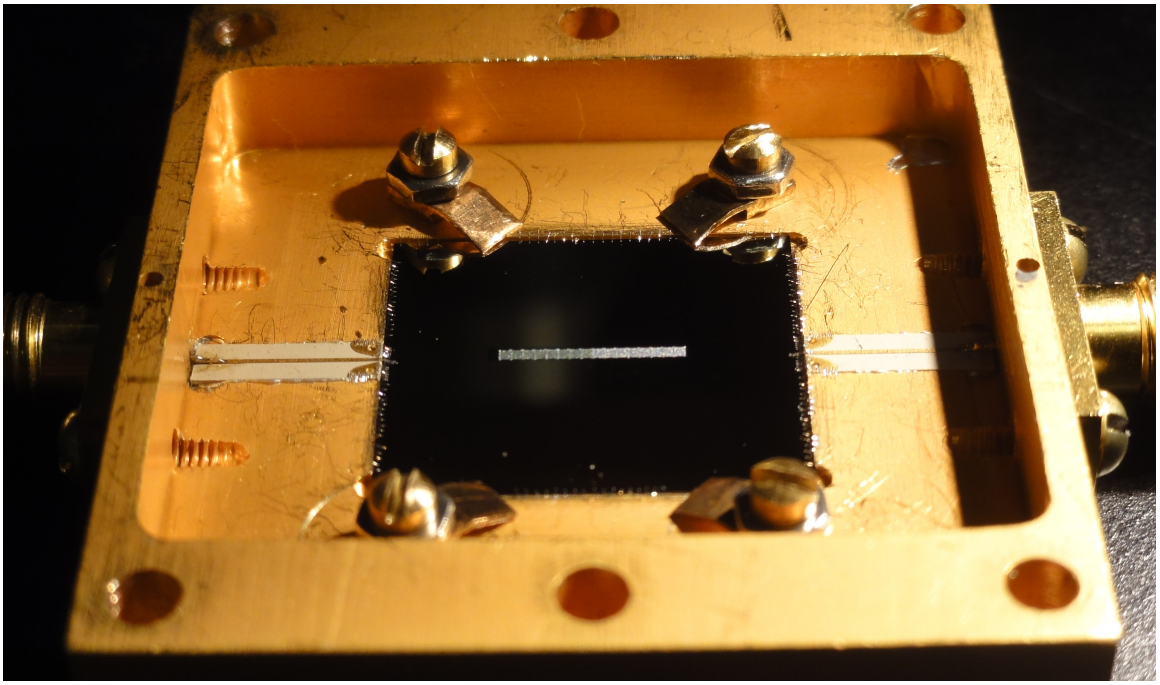

Figure 1.6: The prototype resonator bolometer array studied. The 16 pixels in a row in the center of the substrate are read out by a single transmission line, visible to the left and right of the substrate. The substrate itself is well thermally sunk by multiple wire bonds around its edges.

Chapter 2

Measurement Techniques

2.1 Overview

Several measurements were performed on this prototype array in order to demonstrate its functionality and characterize it fully. Under dark conditions, when the detector is not exposed to light, the temperature dependence of the resonant frequency and quality factor for several pixels was measured. In addition the noise equivalent power (NEP) was obtained as a function of both temperature and readout power. Under illumination, the response of a pixel to a small change in illumination was measured, as well as the NEP and time constant associated with the time taken for the signal to return to baseline upon removal of the radiation source.

2.2 Measurement setup

See Figure 2.1. The basic measurement is a change in amplitude and phase of a tone of a given frequency after interacting with the pixels of the array. A frequency tone is generated by the microwave source and split, with one branch sent straight to a mixer and the other to a transmission line coupled to each pixel, where absorption from a resonance may occur. The two branches are recombined by the mixer, and the two orthogonal components, which can be thought of as the real and imaginary components of the signal, are low pass filtered before being read in by a data acquisition card and saved to file.

Measurements were taken in several distinct runs. For each, the array was first cooled to 4 K via thermal coupling to a liquid helium bath. To achieve temperatures as low as $\sim$1.5 K, we pumped on the helium to lower its boiling point. By varying the pumping strength we could stabilize the temperature anywhere in this 1.5 - 4 K range. The data collection software was written in LabVIEW (Fig. 2.2) and served to automate the data collection process as each independent variable was varied.

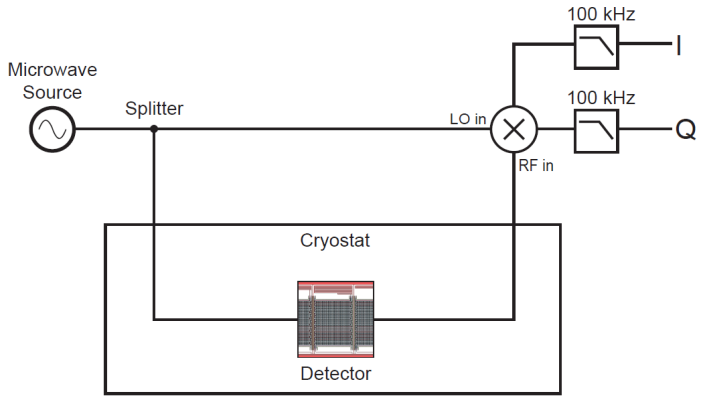

Figure 2.1: Measurement setup. A frequency tone generated by a microwave source is split, with one component traversing the transmission line near the detector pixels, and recombined by a mixer to retrieve orthogonal components of the signal, which are used to calculate amplitude and phase information.

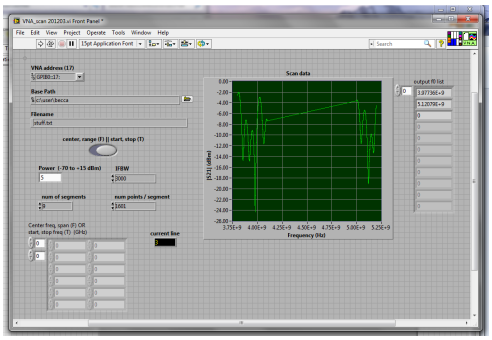

(a) LabVIEW Front Panel

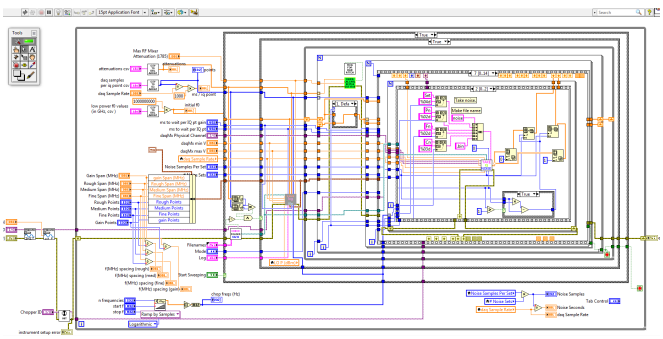

(b) LabVIEW Block Diagram

Figure 2.2: Sample control panel and instrument programming diagram written to control the measurement electronics.

2.3 Fitting for the resonant frequency and quality factor

Sweeping over a range of frequencies, one can reconstruct the resonance profile for a given pixel. Using the standard scattering matrix description of the circuit, the transmitted raw data obeys the relation [6]:

$$S_{21} \equiv I + jQ = a(f)e^{j(\omega\tau+\varphi)}\left(1 - \frac{Q_r}{Q_c}\frac{e^{j\phi}}{1+2jQ_r x}\right), \tag{2.1}$$

where the fractional frequency shift x is given by

$$x = \frac{f - f_{resonance}}{f_{resonance}}. \tag{2.2}$$

In equation (2.1), $a(f)$ represents the frequency-dependent amplitude of the signal if the resonance were absent (the baseline transmission) and $e^{j(\omega\tau+\varphi)}$ is the cable delay term with $\omega = 2\pi f$, τ being the phase shift at f for the cable length present (the cable delay) and φ being the phase at zero frequency. $Q_r = (Q_i^{-1} + Q_c^{-1})^{-1}$ is the total quality factor with Q_i being the internal quality factor and Q_c being the coupling quality factor, and ϕ is an arbitrary phase due to wire bonding. S_{21} is the fraction of power transmitted. Note that Q, the imaginary part of S_{21}, is distinct from the various quality factors Q_r, Q_c and Q_i.

The first steps in solving for the resonance parameters f_r, Q_i and Q_c are to remove the leading factors: the baseline transmission and the cable delay term. By adequately sampling the frequencies near, but not in, the resonance, the cable delay term $\omega\tau + \varphi$ may be fit to a line and the baseline transmission $a(f)$ may be fit to a high degree polynomial (Fig. 2.3 (a), (b)).

Next, the resonance is fit to a circle in the IQ plane (Fig. 2.3 (c)) according to the equation

$$S_{21} = 1 - \frac{Q_r}{Q_c}\frac{e^{j\phi}}{1+2jQ_r x}$$

from which the resonant frequency and quality factors which produce the best fit are found.

While the details differ, this basic procedure and electronic setup was followed for all of the measurements I will describe.

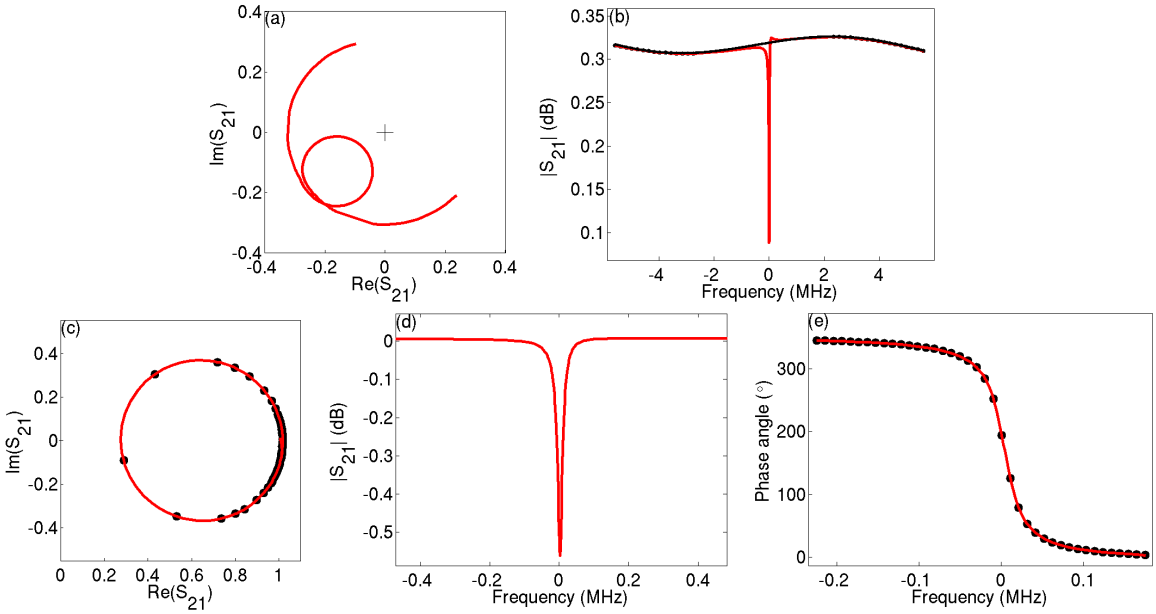

Figure 2.3: Steps in the calibration process. (a) The uncalibrated data traces out a circle centered at the origin for frequencies far from resonance. The resonance is a smaller circle tangent to the large one. (b) Fitting the smooth variation in frequency of the baseline to subtract it from the resonance. (c) The calibrated data, after removing the cable delay and normalizing. The plotted points are equally spaced in frequency. Points at frequencies far from resonance cluster around (1,0). (d) The amplitude and (e) the phase of the calibrated transmitted signal, with the plotted points equally spaced in frequency.

Chapter 3

Dark Measurement Results

The measurements taken can be neatly divided into dark measurements, where the array and cryostat windows were covered to keep optical radiation from reaching the array, and measurements under illumination, where a controlled radiation source was placed in front of the cryostat window to illuminate the detector. Both types of measurement are of interest for characterizing this array; the dark measurements offer a glimpse into the operating capabilities under very low light conditions and allow the most fundamental and characteristic noise sources to dominate and be studied. In contrast the illuminated measurements are more similar to how this array might be used for science so they provide a more concrete picture of the array's potential performance. I will begin by presenting the dark measurement results and later compare these to the illuminated measurement results.

3.1 Temperature dependence

The simplest experiment to carry out is to vary the temperature of the device and record the changes in the resonance. A detector pixel responds to changes in temperature and changes in incident radiation similarly since both processes result in additional Cooper pair-breaking energy in the inductor. Thus we expect to see both the resonant frequency f_r and the quality factor Q_i of the resonance varying with temperature, which was observed (Fig. 3.1). Also shown in the figure is the best fit of a theoretical model based on the Mattis-Bardeen theory of superconductivity. The model is derived in Appendix A. To fit $f_r(T)$, the superconducting transition temperature T_c was allowed to vary; $T_c = 13.7K$ yielded the best fit. $Q_i^{-1}(T)$ depends both on T_c and the kinetic inductance fraction α, defined as the ratio of the kinetic inductance L_k to the total inductance $L_k + L_s$, where L_s is the temperature-invariant geometric inductance. For this fit we fixed T_c at the value determined from the fit to $f_r(T)$ and varied α. $\alpha = 0.55$ gave the best fit.

Finally, the inverse quality factor was plotted against fractional frequency shift to yield Fig. 3.1b. The slope of the fit to the left-most points is β, the ratio of the change in frequency to the change in dissipation from the same signal. Our device has $\beta \sim 35$, indicating the frequency change is larger.

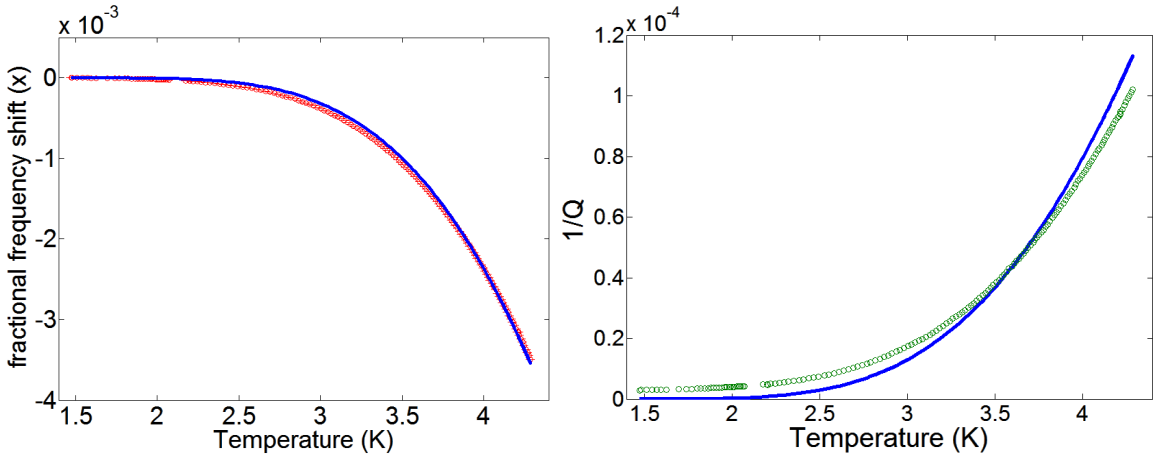

(a) Fractional frequency shift vs. temperature

(b) Quality factor vs. temperature

Figure 3.1: (a) Fractional frequency shift x vs. temperature. The data points are plotted in red, with the fit from Mattis-Bardeen theory (Appendix A) in blue. The fit is a best fit line; the superconducting transition temperature T_c was allowed to vary to find the curve which best matched the data. The shown curve corresponds to $T_c = 13.7K$, which is the value the material was designed to have. (b) Inverse quality factor vs. temperature. The theory predicts that $Q \to \infty$ as $T \to 0$. In this and other superconducting microresonator-based devices however, Q is observed to approach a finite maximum; this is due to other sources of dissipation, including TLS (Section 1.2.5) and radiation into free space [15]. The gap in the data near 2.2 K is the lambda point of liquid helium, where it transitions from superfluid to normal liquid and the associated large change in heat capacity causes a jump in the temperature.

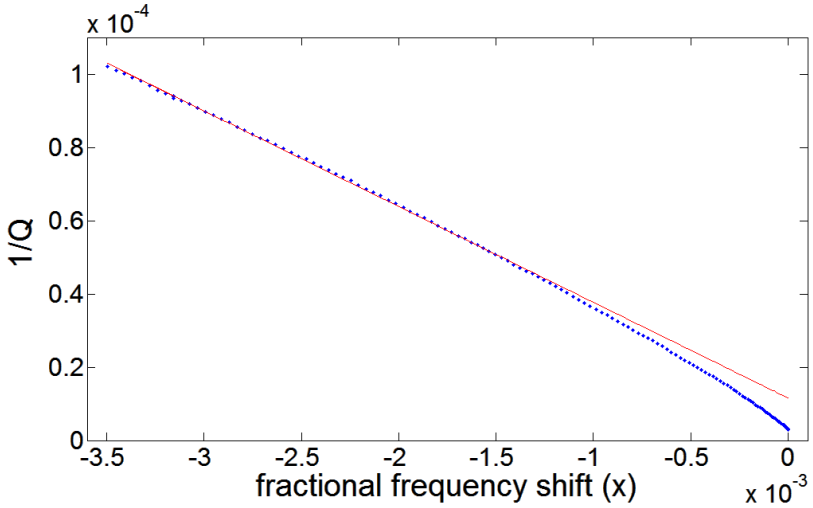

Figure 3.2: Inverse quality factor vs. fractional frequency shift. For the region where Mattis-Bardeen theory is valid, the points map to a line who's slope is β, the ratio of the change in frequency to the change in dissipation from the same signal. Our device has $\beta \sim 35$, indicating the frequency change is much larger.

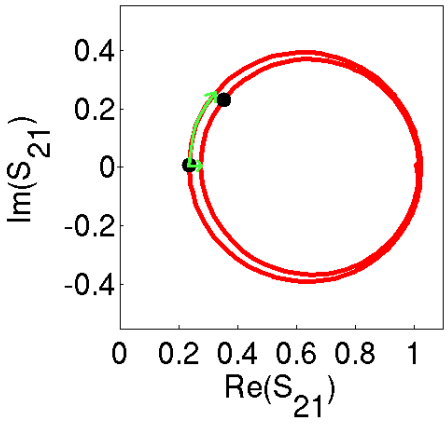

Figure 3.3: To measure a signal change, resonances sampled before and after a change in incident power are compared. The resonant frequency f_r before the change is at a different position after the change; the fractional frequency shift x is thus $(f_{r_{old}} - f_{r_{new}})/f_{r_{new}}$. The signal change in the dissipation direction is also shown.

3.2 Response

With the basic behavior of the resonances understood, the next step was to look toward the measurements necessary to find out the sensitivity of the array. The sensitivity depends both on the magnitude of the response of the resonator to a small change in the incident power and the random fluctuations, or noise, in the resonator properties measured. If the power change results in a response so small that it cannot be distinguished from the random fluctuations, then the detector is not sensitive enough to observe that change. More precisely, the sensitivity for long wavelength detectors is usually given as the noise equivalent power, defined for noise S_{xx} and response R as

$$NEP = \frac{\sqrt{S_{xx}}}{R}. \tag{3.1}$$

Thus accurate measurements of both the response and the noise are necessary to estimate the NEP.

Signal changes are measured by comparing a resonance before and after a small change in the incident power. Because both reactive and dissipative changes occur, either or both of these changes may be measured independently to infer the change in incident power. Changes in the resonant frequency (reactive) are along the resonance loop and dissipation changes are perpendicular to it (Fig. 3.3). The response is significantly larger in the frequency direction as a consequence of superconductivity theory. This makes the frequency direction less susceptible to electronic noise; for this reason, we focus on the response and noise measurements in the frequency direction only. The signal change produces a response in the form of a fractional frequency shift x, given by Eq. (2.2). Note that in a system where this detector is used for science applications, both directions may be used.

The response was measured with and without light allowed into the cryostat. In the former case,

the mechanism is straightforward; a change in the incident power causes changes in the resonance as described above. In the latter case, small temperature changes serve as the effective signal. These may be converted to equivalent changes in incident power by G, the thermal conductance of the bolometer island legs:

$$G\Delta T = \Delta P.$$

The response under dark conditions is thus

$$R = \frac{\Delta x}{G\Delta T}.$$

3.2.1 Thermal conductance calculation

$x/\Delta T$, the response to temperature changes, is readily calculated as the derivative of the curve in Fig. 3.1a. The other necessary quantity is the thermal conductance G of the bolometer island legs. It is known empirically that G exhibits a roughly T^3 dependence [1]. From the phonon NEP expression given in Section 1.1.1 and Eq. (3.1), we can solve for G:

$$G = \frac{4k_B T^2 (\Delta x/\Delta T)^2}{S_{xx}^{\text{phonon}}}$$

where S_{xx}^{phonon} is the phonon contribution to the total noise S_{xx}. Measurements of the phonon noise (see Section 3.3.3 below) fit to a T^3 power law yield, in nW/K,

$$G \approx 0.3T^3.$$

3.2.2 Results

The response is shown as a function of temperature in Fig. 3.4. Importantly, there is well over an order of magnitude difference between the response at 1.5 K and at 4 K, suggesting that the lowest temperatures will not yield the optimal sensitivity.

3.3 Noise

3.3.1 Data collection and processing

The noise is first measured by sampling a resonance and then outputting a single tone from the signal generator at the resonant frequency. Sampling at this position for several seconds yields a spread of data points representing the noise (Fig. 3.5). Like the response, the noise may be measured in either the frequency direction or the dissipation direction, or both; we chose the frequency direction

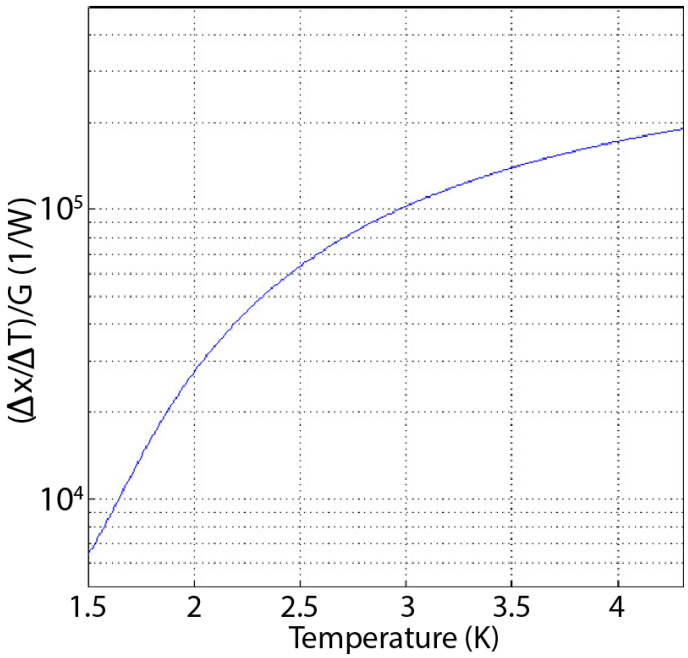

Figure 3.4: Calculated response from $G = 0.3T^3$ nW/K.

for reasons stated above (Sec. 3.2). From the initial scan of the resonance, a mapping between the generator frequencies and the points on the resonance loop is made, and the fractional frequency shift x for each point is calculated (Eq. (2.2)).

Next, the power spectral density of the time stream of data is computed. The power spectral density quantifies the power carried by each frequency component of a stochastic process (in this case, the noise data stream) and is typically given in Watts/Hz. This is normalized by dividing by the total power in the signal to yield the fractional frequency noise S_{xx} in $(\text{Hz})^{-1}$.

3.3.2 Noise sources

A typical set of noise plots for one pixel are shown in Figure 3.6. Several distinct processes contribute to the observed noise. Phonon noise from quantized fluctuations in thermal energy in the bolometer island legs (section 1.1.1) introduce noise up to about 150 Hz, where the noise is low-pass filtered by the thermal time constant τ (see sections 1.1 and 4.2). At lower frequencies, electronics and thermal instability associated with pumping on a liquid helium bath increase the noise. At the highest frequencies, two different noise sources dominate at different temperatures. At low T, two level system noise (see section 1.2.5) dominates. It is low-pass filtered by the resonator ring-down time constant (see Appendix B). At high T the resonator Q decreases significantly. This leads to a relatively increased electronic contribution at high noise frequencies ($>\sim$ 1kHz). It, along with all the other noise sources, is rolled off by an anti-aliasing 100 kHz low-pass filter. Finally, the sharp noise spikes originate from the electronics.

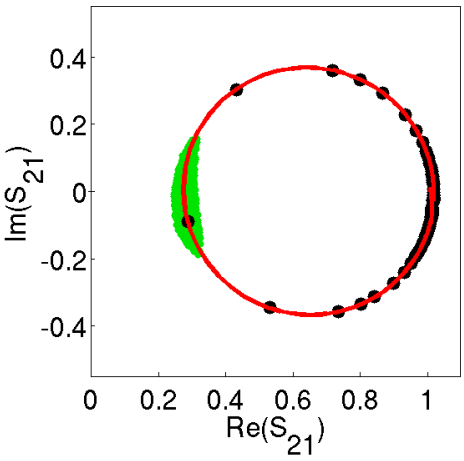

Figure 3.5: Noise at resonance. Each data point in the green spread is mapped to a frequency using the fit to a frequency scan over the resonance (black points).

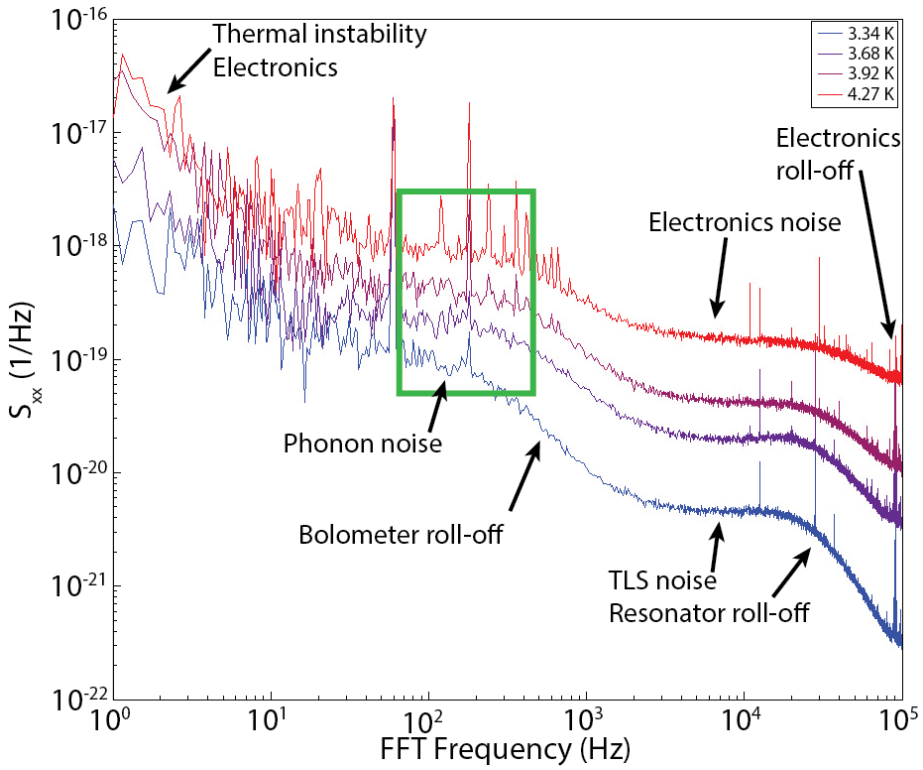

Figure 3.6: Example fractional frequency noise plots at various temperatures. The green box indicates the frequencies of interest for the NEP calculation; higher frequencies will not be used for science applications and non-detector-based noise takes over at lower frequencies.

3.3.3 Dark noise results

In practice, signals varying with frequencies above the bolometer roll-off cannot be observed with this detector because the averaging effect of the bolometer time constant will reduce the signal. Thus the frequencies of interest for operation are $\sim$ 150 Hz and below. Extraneous noise from thermal drift and excess noise exhibited by our cryogenic amplifier dominate at very low frequencies. In the future, these can be greatly reduced with a new amplifier and a thermally controlled sample stage. For this measurement however, the value of S_{xx} used to calculate the NEP is an average of the data points within the green box in Fig. 3.6, excluding the electronic noise spikes. This average noise is plotted vs. temperature in Fig. 3.7. A clear minimum is visible at $\sim$ 2.5 K; to either side, the two most important noise sources dominate. At high temperatures, the phonon noise dominates; it is given by

$$S_{xx}^{\text{phonon}} = \frac{4k_B T^2 (\Delta x/\Delta T)^2}{G}.$$

The plotted phonon noise curve is a best fit of this equation to the data, with G as a variable parameter. $G = 0.3T^3$ nW/K yields the best fit; thus this was the dependence chosen for the response calculation (section 3.2).

At the low temperature end, the TLS noise dominates due to its T^{-2} dependence. The exact proportionality constant for this dependence was also chosen for its fit to the data; thus

$$S_{xx}^{\text{TLS}} = \frac{3 * 10^{-19}\ \text{K}^2/\text{Hz}}{T^2}.$$

Added together, these two sources predict the temperature dependence of the noise nicely. The next step is to combine the noise data with the response data to get the NEP. This is done at the end of chapter 4 together with the NEP under illuminated conditions.

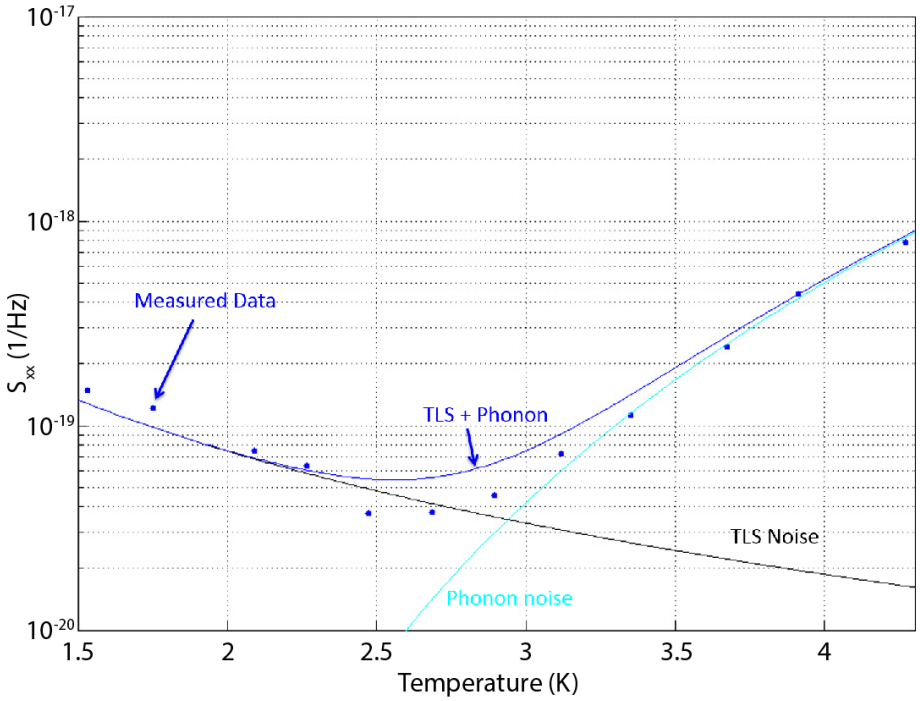

Figure 3.7: Noise under dark conditions. Phonon noise dominates at high temperatures, while TLS noise dominates at low temperatures.

Chapter 4

Measurements under illumination

Up to this point I have discussed only the dark measurements. While most of the procedure remains the same for the corresponding measurements under illumination, particularly the data processing, the experimental setup changes significantly with the addition of an external light source. In this chapter I will explain some of these extra procedural challenges and present the results in comparison with the corresponding dark measurement.

4.1 Optical response measurement

When light is allowed into the cryostat, a change in the power radiated by an optical source leads to changes in x. In this case the response is simply

$$R = \frac{\Delta x}{\Delta P}.$$

The changes ΔP were produced by placing a chopper wheel between a voltage-controlled blackbody and the cryostat window (Fig. 4.1). The chopper wheel was placed behind a sheet of room-temperature absorbing material with a small hole to define the aperture. As the chopper wheel spun, it alternately blocked and passed light from the blackbody behind it, producing an approximately square wave signal of amplitude ΔP. The corresponding frequency changes were recorded as a function of operating temperature and the results are presented in Fig. 4.2.

4.2 Time Constant

While measuring the bolometer time constant is not necessary for computing the NEP, it remains a physically interesting measurement, since it tells us what kinds of time-varying signals we can observe. This measurement is conceptually similar to the response measurement, since in both cases the response of the resonator to a pulse of light is recorded. In this case, we were focusing on the transitions of the resonator to and from its baseline in response to the pulse. A terahertz

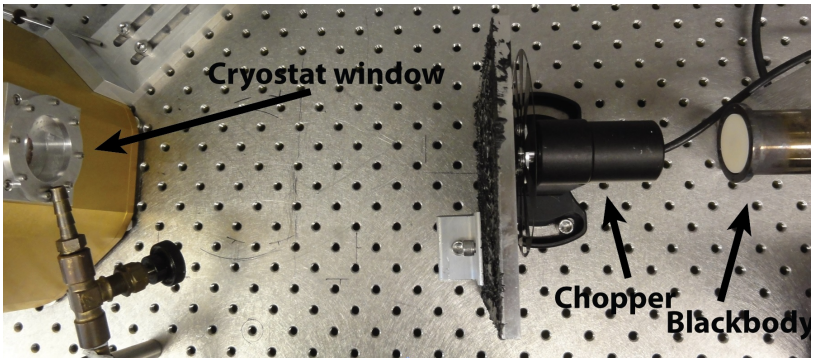

Figure 4.1: Setup for the optical response measurement. Light from a blackbody held at a fixed temperature is modulated by the rotation of the chopper wheel. An aluminum plate covered in an absorbing material placed in front of the chopper with a small hole for the aperture ensures that off-axis radiation entering the cryostat comes from a homogeneous source.

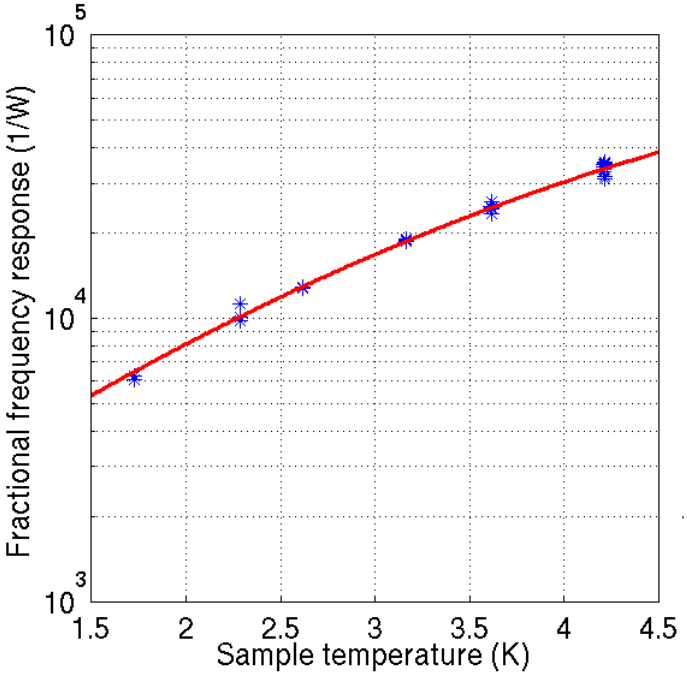

Figure 4.2: Response vs. temperature under optical loading, with a polynomial fit to the data.

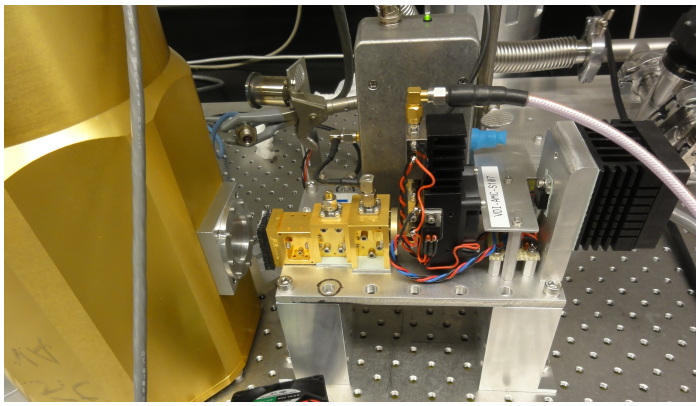

Figure 4.3: Setup for the time constant measurement. A terahertz radiation source was used to ensure that the transitions between low and high intensity were fast compared to the bolometer time constant.

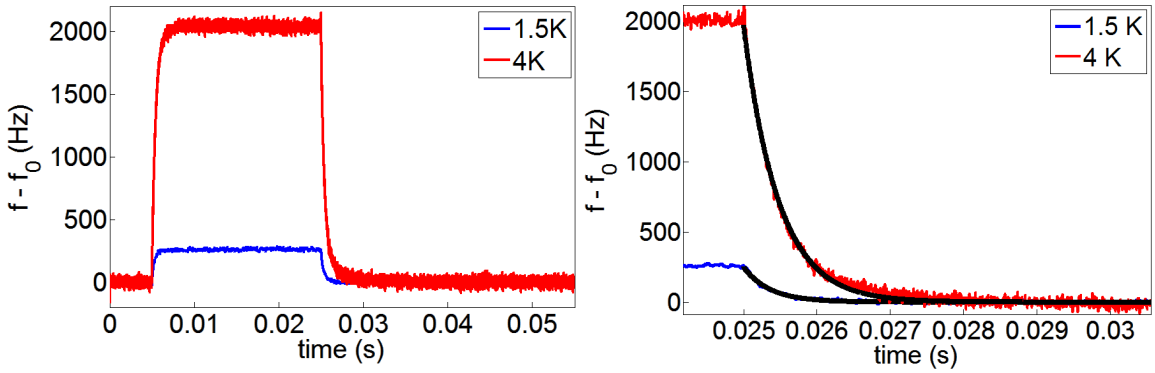

(a) Response to a pulse of THz radiation

(b) Fit to the response decay

Figure 4.4: (a) Responses at low and high operating T to the THz pulse show the substantial difference in the magnitude of the response at these two temperatures. (b) The rise and decay curves may be fit to an exponential (black curves) to estimate the time constant. $\tau_{4K} = 475\mu$s and $\tau_{1.5K} = 365\mu$s.

radiation source was used in place of the blackbody and chopper setup to ensure that sharp square pulses were produced when compared to the bolometer time constant (Fig. 4.3).

Sample pulses are shown in Fig. 4.4a. The difference in response between 1.5 K and 4 K is clearly visible. Also evident are the exponential rise and decay of the frequency shift. Fitting the decay curves to an exponential function (Fig. 4.4b) yields $\tau_{4K} = 475\mu$s and $\tau_{1.5K} = 365\mu$s; these values agree with the value that may be estimated from the phonon noise roll-off in the noise plots (sections 3.3.2 and 4.3).

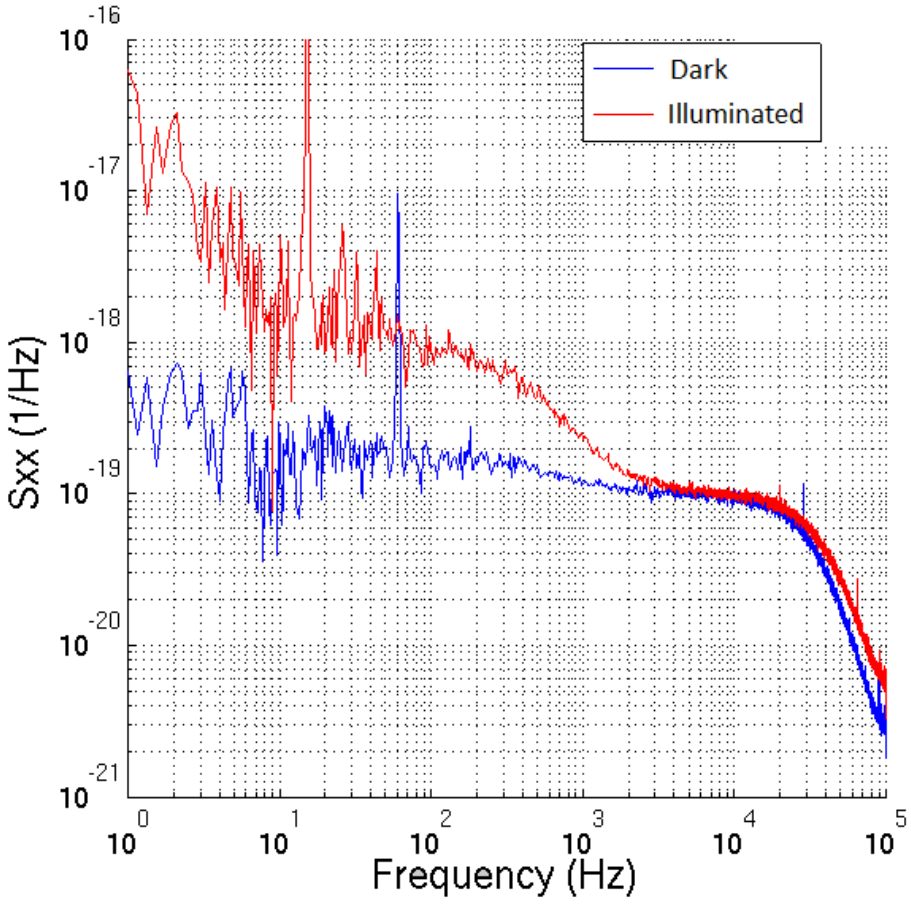

Figure 4.5: Noise plots for a single pixel at a constant temperature ($\sim$ 3 K). While the overall structure is similar, the noise under illumination is higher below the phonon noise roll-off, reflecting the presence of photon noise.

4.3 Noise under illumination

Fig. 4.5 compares two noise plots taken at the same temperature for the same pixel under dark and illuminated conditions. Evidently the structure is the same; both measurements clearly exhibit low frequency thermal instability noise, a phonon noise roll-off between 10^2 and 10^3 Hz, and in this case TLS noise rolled off by the resonator ring-down time (Appendix B) at high frequencies. However, in the illuminated case the noise is higher below the phonon noise roll-off; this reflects the addition of photon noise, which has no intrinsic spectral dependence but which is rolled off by the detector response.

When we again average the noise around 150 Hz over multiple temperatures, we see the added photon noise contribution in the optical data when compared with the dark data (Fig. 4.6). Assuming a constant photon NEP, the photon noise may be calculated:

$$S_{xx}^{\text{photon}} = (\text{NEP}_{\text{photon}} * (\Delta x/\Delta T))^2.$$

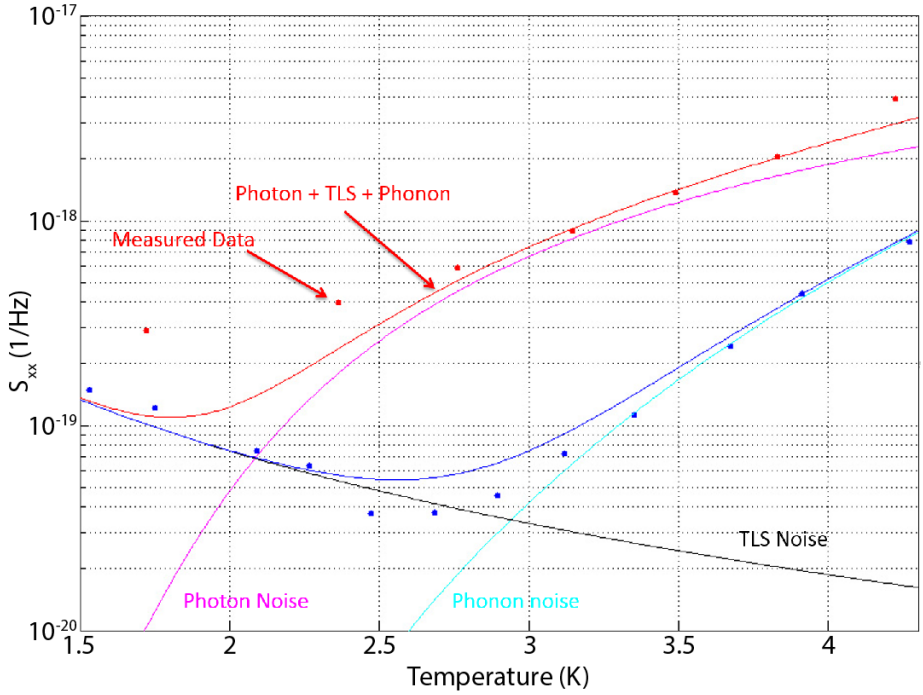

Figure 4.6: Noise vs. temperature at 150 Hz. The red data points are the noise under illumination while the blue data points are under dark conditions. Adding a constant photon NEP modulated by the response of the detector and added to the phonon and TLS noise determined from the dark data produces good agreement with the data for $T > 2.5$K.

$\text{NEP}^{\text{photon}} = 8{*}10^{-15}$ W/Hz$^{1/2}$ produces the best fit to the data. The photon noise is added to the phonon and TLS noise as fit from the dark data.

4.4 Noise equivalent power

The noise equivalent power (NEP) in terms of the fractional frequency noise and response is

$$NEP = \frac{\sqrt{S_{xx}}}{R}.$$

The dark and illuminated NEP are plotted together with the photon NEP in Figure 4.7. A clear minimum is present in the dark NEP around 3 K and to some extent also in the illuminated NEP. The upward trend as temperature decreases reflects the diminishing response, while in the opposite direction phonon and photon noise dominate.

The plot highlights a discrepancy in our data which is currently under investigation. The photon NEP was calculated from a fit to the noise as described in section 4.3. Thus, assuming the response was calculated correctly, the NEP under illumination should equal the sum of the photon and dark NEPs. This is not the case, implying the response calculation is not taking everything into account. The greatest source of uncertainty is our estimated value of ΔP for the response calculation; the

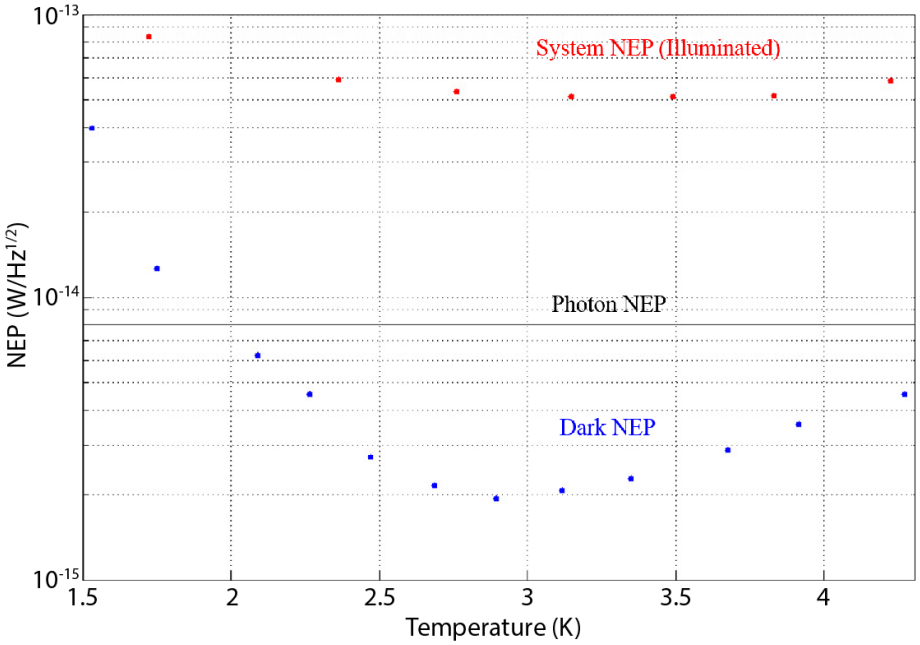

Figure 4.7: Noise equivalent power under dark and illuminated conditions as compared to the calculated photon NEP. A NEP minimum is established around 3 K. The discrepancy between the photon NEP and the measured NEP under illumination is currently being investigated.

discrepancy observed in Fig. 4.7 suggests that light is being absorbed by the detector than originally taken into account. ΔP is the power absorbed by the detector, and as such depends on (1) the optical load entering the cryostat, (2) the characteristics of the filters in the light path, and finally (3) the spectral dependence of the detector absorption. (2) and (3) are currently uncertain and under investigation: (2) because out of band transmission may contribute significantly to the detector loading, and (3) because, as this is a novel prototype device, the resonator bolometer's absorption properties have been neither measured experimentally nor modeled. I am currently working on modeling the device absorption. Appendix C details the analytic solution to the simplest case. Starting with this simplest case, I have been using finite element structure simulator software to approximate the device design.

Chapter 5

Conclusion

The measurements presented here form a comprehensive characterization of the resonator bolometer array and point towards several avenues of further research. Design changes have been proposed which would improve the device performance. For example, depositing the capacitor directly onto the silicon substrate instead of on a layer of silicon nitride should substantially reduce the TLS noise. Additionally, other superconducting microresonator detector projects have begun to engineer the resonances at much lower frequencies in order to eliminate the need for an analog mixer. Removing this analog component not only reduces complexity but significantly reduces cost and removes a potential source of electronic noise from the system. Finally, investigations into increased optical coupling will help ready this device for science applications.

One of the initial uses envisioned for this technology is in climate monitoring of the Earth from a satellite in low-earth orbit. For this application, the loading conditions measured in the laboratory and presented here are similar. Under these conditions the device has been shown to be photon-noise limited with sufficient dynamic range and is therefore nearly an ideal device. To increase the mapping speed, the optical efficiency of the detector needs to be improved and we are actively working on this aspect of the device.

Appendix A

Expressions for $f_r(T)$ and $Q_i(T)$ from Mattis-Bardeen theory

The Mattis-Bardeen theory of the anomalous skin effect in superconductors [10] may be used to derive the behavior of the resonance as the superconductor's temperature is varied.

A.1 Temperature dependence of f_r

Given conductivity $\sigma_s = \sigma_1 - i\sigma_2$, the superconducting resistivity is

$$\rho_s \equiv \frac{1}{\sigma_s} = \frac{\sigma_1 + i\sigma_2}{\sigma_1^2 + \sigma_2^2}.$$

The superconducting resistance is thus

$$R_s = \frac{\sigma_1}{\sigma_1^2 + \sigma_2^2} R_N$$

where R_N is the resistance in the normal state. Likewise, the superconducting inductance is given by

$$\omega L_s = \frac{\sigma_2}{\sigma_1^2 + \sigma_2^2} R_N$$

where ω is the angular frequency. The resonant frequency of an LC circuit is

$$2\pi f_r = \omega_r = \frac{1}{\sqrt{LC}}.$$

Let f_0 be the resonant frequency of the circuit at 0K. Then

$$x \equiv \frac{f_r - f_0}{f_0} = \frac{f_r}{f_0} - 1 = \sqrt{\frac{(L_r C)^{-1}}{(L_0 C)^{-1}}} - 1 = \sqrt{\frac{L_0}{L_r}} - 1$$

$$= \sqrt{\frac{\sigma_{2_0}}{\omega_0(\sigma_{1_0}^2 + \sigma_{2_0}^2)} \frac{\omega_r(\sigma_{1_r}^2 + \sigma_{2_r}^2)}{\sigma_{2_r}}} - 1.$$

Because we are dealing with frequency changes on the order of a few thousandths of f_0 (i.e. a few MHz), $\omega_r/\omega_0 \approx 1$. Also, for $T \ll T_c$, $\sigma_2 \gg \sigma_1$, so $\sigma_1^2 + \sigma_2^2 \approx \sigma_2^2$. Using these approximations, we have:

$$x \approx \sqrt{\frac{\sigma_{2_r}}{\sigma_{2_0}}} - 1.$$

σ_2 is related to the temperature by

$$\frac{\sigma_2(\omega)}{\sigma_n} = \frac{1}{\hbar\omega} \int_{\Delta}^{\Delta+\hbar\omega} dE \frac{E^2 + \Delta^2 - \hbar\omega E}{\sqrt{E^2 - \Delta^2}\sqrt{\Delta^2 - (E - \hbar\omega)^2}} [1 - 2f(E)], \tag{A.1}$$

where σ_n is the normal state conductivity, $\Delta \approx 3.5 k_B T_c$ is half the Cooper pair binding energy, ω is the angular resonant frequency and $f(E)$ is the distribution function for quasiparticles, given by $f(E) = 1/(e^{E/kT} + 1)$ in thermal equilibrium.

A.2 Temperature dependence of Q_i

The internal quality factor Q_i is the ratio of ω times the kinetic inductance L_k to the resistance R_s in the circuit. The kinetic inductance fraction $\alpha \equiv L_k/L_s$. Using the equations for R_s and ωL_s in section A.1, we can express Q_i as a function of σ_1 and σ_2:

$$Q_i = \frac{\omega L_k}{R_s} = \frac{1}{\alpha}\frac{\omega L_s}{R_s} = \frac{1}{\alpha}\frac{\sigma_2}{\sigma_1}.$$

σ_2 is given by Equation (A.1), while

$$\frac{\sigma_1(\omega)}{\sigma_n} = \frac{2}{\hbar\omega} \int_{\Delta}^{\infty} dE \frac{E^2 + \Delta^2 + \hbar\omega E}{\sqrt{E^2 - \Delta^2}\sqrt{(E + \hbar\omega)^2 - \Delta^2}} [f(E) - f(E + \hbar\omega)]$$

with the quantities σ_n, Δ, ω and $f(E)$ defined in section A.1.

Appendix B

Resonator ring-down time derivation

The total quality factor Q_r is given by:

$$Q_r = \frac{\omega_0 \epsilon}{P}$$

where $\omega_0 = 2\pi f_0$ is the angular resonant frequency, $\epsilon = \frac{1}{2} L I^2$ is the energy stored in the resonance and $P = \frac{1}{2} I^2 R$ is the power dissipated. Plugging in for ϵ and P yields:

$$Q_r = \frac{\omega_0 \frac{1}{2} L I^2}{\frac{1}{2} I^2 R} = \frac{\omega_0 L}{R}$$

The attenuation can be obtained by solving the equation of motion for an RLC circuit and is equal to $\frac{R}{2L}$. Then we have:

$$\text{attenuation} = \frac{R}{2L} = \frac{\omega_0}{2} \frac{R}{\omega_0 L} = \frac{\omega_0}{2} \frac{1}{Q_r} = \frac{2\pi f_0}{2 Q_r} = \frac{\pi f 0}{Q_r}$$

The resonator ring-down time τ_{res} is defined as the inverse of attenuation, so, in terms of quantities easily found from fitting resonances,

$$\boxed{\tau_{res} = \frac{Q_r}{\pi f_0}}. \tag{B.1}$$

τ_{res} can also be expressed in terms of the bandwidth Δf by substituting $Q_r = \frac{f_0}{\Delta f}$:

$$\tau_{res} = \frac{1}{\pi \Delta f}.$$

Physically, the resonator ring-down time is the timescale on which the resonator loses energy during oscillation. By design, the bolometer time constant (sec 4.2) is much greater than the resonator ring-down time, so that quantity dominates in our measurements.

Appendix C

HFSS modeling calculations

An accurate NEP under loading can only be determined if the optical power reaching the detector is well known. This requires knowledge of both the absorption of the filters in front of the detector and the spectral dependence of the absorption of the detector itself. The former is provided by specification sheets for the filters, but the latter must be measured or modeled. In order to confidently report the amount of radiation absorbed by the detector, we have modeled the absorption of a single pixel. Details of the methodology are reported here.

C.1 Description of circuit

See section 1.3.1.

C.2 Analytic solution to simplest case

The simplest approximation treats the meandering inductor as a uniform 80 Ω sheet resistance on one surface of the silicon substrate in free space (see Fig. C.1). The Si substrate has a thickness of $l = 500$ μm. Standing waves can occur in the silicon. Maximum transmission occurs when the

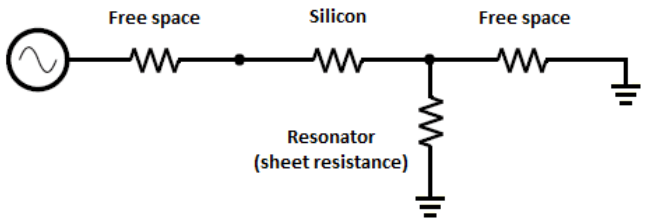

Figure C.1: In the simplest approximation, the light sensitive part of the resonator, the meandering inductor, is treated as a sheet resistance on the boundary between the silicon substrate and free space.

substrate thickness is an odd integer multiple of a quarter of a wavelength. Minimum transmission occurs when the substrate thickness is an even integer multiple of a quarter of a wavelength. To find the frequencies of minimum and maximum transmission, we evaluate:

$$\frac{n\lambda}{4} = \frac{n}{4}\frac{c}{\nu\sqrt{\epsilon}}$$

where $\lambda/4 = l = 500\mu$m and $\epsilon_{Si} = 11.9$. Solving yields

$$n\nu = n * 4.35 * 10^{10}\text{Hz}.$$

In the case that n is even, we are dealing with half-wavelength multiples, so the magnitude of the voltage is the same at either end of the silicon section. This means we can eliminate it from the circuit. The simplified circuit is free space in series with free space and a 50 Ω sheet resistance to ground in parallel. The equivalent impedance for the parallel section is

$$\frac{1}{\frac{1}{50\Omega} + \frac{1}{377\Omega}} = 44.1\ \Omega.$$

And the reflection coefficient for the transition between free space and this load is

$$\Gamma_{\frac{1}{2}\lambda} = \frac{377 - 44.1}{377 + 44.1} = 0.79.$$

In the case that n is odd, the equivalent impedance of the Si section plus load (free space in parallel with 50 Ω sheet resistance) is Z_{Si}^2/Z_{load}, so that the reflection coefficient is

$$\Gamma_{\frac{1}{4}\lambda} = \frac{377 - (377/\sqrt{11.9})^2/44.1}{377 + (377/\sqrt{11.9})^2/44.1} = 0.16.$$

|S11| should oscillate between these two extremes.

Bibliography

[1] Neil W. Ashcroft and N. David Mermin. *Solid State Physics*. Harcourt College Publishers, 1976.

[2] J. Bardeen, L. N. Cooper, and J. R. Schrieffer. Theory of Superconductivity. *Physical Review*, 108(5):1175–1204, 1957.

[3] R. Barends, H. L. Hortensius, T. Zijlstra, J. J. A. Baselmans, S. J. C. Yates, J. R. Gao, and T. M. Klapwijk. Contribution of dielectrics to frequency and noise of NbTiN superconducting resonators. *Applied Physics Letters*, 92(22), JUN 2 2008.

[4] Collaboration for Astronomy Signal Processing and Electronics Research. ROACH, February 2012. `https://casper.berkeley.edu/wiki/ROACH`.

[5] P. K. Day, H. G. LeDuc, B. A. Mazin, A. Vayonakis, and J. Zmuidzinas. A broadband superconducting detector suitable for use in large arrays. *Nature*, 425(6960):817–821, OCT 23 2003.

[6] Jiansong Gao. *The Physics of Superconducting Microwave Resonators*. PhD thesis, California Institute of Technology, 2008.

[7] Jiansong Gao, Miguel Daal, John M. Martinis, Anastasios Vayonakis, Jonas Zmuidzinas, Bernard Sadoulet, Benjamin A. Mazin, Peter K. Day, and Henry G. Leduc. A semiempirical model for two-level system noise in superconducting microresonators. *Applied Physics Letters*, 92(21), MAY 26 2008.

[8] Jiansong Gao, Jonas Zmuidzinas, Benjamin A. Mazin, Henry G. LeDuc, and Peter K. Day. Noise properties of superconducting coplanar waveguide microwave resonators. *Applied Physics Letters*, 90(10), MAR 5 2007.

[9] Henry G. Leduc, Bruce Bumble, Peter K. Day, Byeong Ho Eom, Jiansong Gao, Sunil Golwala, Benjamin A. Mazin, Sean McHugh, Andrew Merrill, David C. Moore, Omid Noroozian, Anthony D. Turner, and Jonas Zmuidzinas. Titanium nitride films for ultrasensitive microresonator detectors. *Applied Physics Letters*, 97(10), SEP 6 2010.

[10] D. C. Mattis and J. Bardeen. Theory of the Anomalous Skin Effect in Normal and Superconducting Metals. *Physical Review*, 111(2):412–417, 1958.

[11] Sean McHugh, Benjamin A. Mazin, Bruno Serfass, Seth Meeker, Kieran O'Brien, Ran Duan, Rick Raffanti, and Dan Werthimer. A readout for large arrays of microwave kinetic inductance detectors. *Review of Scientific Instruments*, 83(4), APR 2012.

[12] D. C. Moore, S. Golwala, B. Bumble, B. Cornell, B. A. Mazin, J. Gao, P. K. Day, H. G. LeDuc, and J. Zmuidzinas. Phonon Mediated Microwave Kinetic Inductance Detectors. *Journal of Low Temperature Physics*, 167(3-4, Part 1):329–334, MAY 2012. 14th International Workshop on Low Temperature Particle Detection (LTD), Heidelberg Univ, Kirchhoff-Inst Phys, Heidelberg, GERMANY, AUG 01-05, 2011.

[13] P. L. Richards. Bolometers for infrared and millimeter waves. *Journal of Applied Physics*, 76(1):1–24, 1994.

[14] A Wallraff, DI Schuster, A Blais, L Frunzio, RS Huang, J Majer, S Kumar, SM Girvin, and RJ Schoelkopf. Strong coupling of a single photon to a superconducting qubit using circuit quantum electrodynamics. *Nature*, 431(7005):162–167, SEP 9 2004.

[15] Jonas Zmuidzinas. Superconducting Microresonators: Physics and Applications. In Langer, JS, editor, *Annual Review of Condensed Matter Physics, VOL 3*, volume 3 of *Annual Review of Condensed Matter Physics*, pages 169–214. ANNUAL REVIEWS, 4139 EL CAMINO WAY, PO BOX 10139, PALO ALTO, CA 94303-0897 USA, 2012.